EPJ manuscript No.
(will be inserted by the editor)

$K^0\pi^0\Sigma^+$ and $K^{*0}\Sigma^+$ photoproduction off the proton

M. Nanova[1], J. C. S. Bacelar[2], B. Bantes[3], O. Bartholomy[4], D. Bayadilov[4,5], R. Beck[4], Y.A. Beloglazov[5], R. Castelijns[2,a], V. Crede[6], H. Dutz[3], A. Ehmanns[4], D. Elsner[3], K. Essig[4], R. Ewald[3], I. Fabry[4], K. Fornet-Ponse[3], M. Fuchs[4], Ch. Funke[4], R. Gothe[3,b], R. Gregor[1], A. B. Gridnev[5], E. Gutz[4], P. Hoffmeister[4], I. Horn[4], I. Jaegle[7], J. Junkersfeld[4], H. Kalinowsky[4], S. Kammer[3], V. Kleber[3], Frank Klein[3], Friedrich Klein[3], E. Klempt[4], M. Konrad[3], M. Kotulla[1], B. Krusche[7], M. Lang[4], J. Langheinrich[3,b], H. Löhner[2], I.V. Lopatin[5], J. Lotz[4], S. Lugert[1], D. Menze[3], J. G. Messchendorp[2], T. Mertens[7], V. Metag[1], C. Morales[3], D.V. Novinski[5], R. Novotny[1], M. Ostrick[3,c], L. M. Pant[1,d], H. van Pee[4], M. Pfeiffer[1], A. Radkov[5], A. Roy[1,e], S. Schadmand[1,a], Ch. Schmidt[4], H. Schmieden[3], B. Schoch[3], S. V. Shende[2], V. Sokhoyan[4], A. Süle[3], V. V. Sumachev[5], T. Szczepanek[4], U. Thoma[1,4], D. Trnka[1], R. Varma[1,e], D. Walther[3,4], Ch. Weinheimer[4,f], and Ch. Wendel[4]
(The CBELSA/TAPS Collaboration)

[1]II. Physikalisches Institut, Universität Gießen, Germany
[2]Kernfysisch Versneller Institut, Groningen, The Netherlands
[3]Physikalisches Institut, Universität Bonn, Germany
[4]Helmholtz-Institut für Strahlen- u. Kernphysik, Universität Bonn, Germany
[5]Petersburg Nuclear Physics Institute, Gatchina, Russia
[6]Department of Physics, Florida State University, Tallahassee, FL, USA
[7]Physikalisches Institut, Universität Basel, Switzerland
[a]Present address: Forschunszentrum Jülich, Germany
[b]Present address: University of South Carolina, Columbia, SC, USA
[c]Present address: Universität Mainz, Germany
[d]Present address: BARC, Mumbai, India
[e]Present address: I.I.T. Powai, Mumbai, India
[f]Present address: Universität Münster, Germany

Received: date / Revised version: date

Abstract. The exclusive reactions $\gamma p \to K^{*0}\Sigma^+(1189)$ and $\gamma p \to K^0\pi^0\Sigma^+(1189)$, leading to the p $4\pi^0$ final state, have been measured with a tagged photon beam for incident energies from threshold up to 2.5 GeV. The experiment has been performed at the tagged photon facility of the ELSA accelerator (Bonn). The Crystal Barrel and TAPS detectors were combined to a photon detector system of almost 4π geometrical acceptance. Differential and total cross sections are reported. At energies close to the threshold, a flat angular distribution has been observed for the reaction $\gamma p \to K^0\pi^0\Sigma^+$ suggesting dominant s-channel production. $\Sigma^*(1385)$ and higher lying hyperon states have been observed. An enhancement in the forward direction in the angular distributions of the reaction $\gamma p \to K^{*0}\Sigma^+$ indicates a t-channel exchange contribution to the reaction mechanism. The experimental data are in reasonable agreement with recent theoretical predictions.

PACS. 13.60.Le Meson production – 25.20.Lj Photoproduction reactions – 14.20.Jn Hyperons

1 Introduction

The internal structure of the nucleon is reflected in the rich pattern of baryon resonances. The number of experimentally observed resonances is much smaller than predicted from theory [1]. This is often referred to as the 'missing' resonance problem. Baryon resonances have often large widths and overlap largely, which makes the study of the excited states particularly difficult. It is possible to overcome this problem by looking at specific decay channels. Up to now most existing data are based on elastic πN scattering experiments. If the hypothesis is correct that the missing states are unobserved because they couple weakly to the πN decay channel, it may be possible to establish some of these missing states in other channels. Some of the resonances are predicted to decay into final states with strange particle pairs, coupling strongly to $K\Lambda$ and $K\Sigma$ [2]. Strangeness production experiments will therefore be an important tool to establish 'missing' resonances and

Correspondence to: Mariana.Nanova@physik.uni-giessen.de

their properties or to disprove their existence. Recently new measurements of differential and total cross sections of hyperon photoproduction have been reported by the SAPHIR [3], LEPS [4], CBELSA/TAPS [5] and CLAS [6, 7] collaborations. A partial wave analysis provided a good description of these data by introduction of a new state with P_{13} quantum numbers and two solutions for the mass - either at 1885 MeV or at 1970 MeV [8,9].

Higher mass nucleon resonances could favour decays into $K^*\Sigma$. Therefore K^* vector meson photoproduction can be used to search for nucleon resonances which couple strongly to the K^*Y channel, where Y denotes a hyperon [10]. On the other hand, photoproduction of K^* shares elements in common with other strangeness production reactions, such as $\gamma p \to K\Lambda$ and $\gamma p \to K\Sigma$ or $\gamma p \to \pi K\Sigma$, which lead to N^* or to N^* and Δ^* resonance excitations with different couplings. The investigation of higher lying hyperon Σ^* resonances will provide more information about the baryon resonances in meson-hyperon decay channels and help to understand their contribution as background to K^* photoproduction in the reaction $\gamma p \to K^{*0}\Sigma^+$.

The cross sections for these reaction channels are small and their experimental identification is difficult. Therefore their investigation became only feasible when high quality photon beam facilities combined with 4π high resolution detectors became available. Here we present the experimental data of $\Sigma^+(1189)$ photoproduction off the proton by analysing:

(1) $\gamma p \to \pi^0 K^0 \Sigma^+ \to \pi^0(\pi^0\pi^0)(\pi^0 p) \to 8\gamma p$

This reaction contains the following isobars:

(2) $\gamma p \to K^{*0}\Sigma^+$

(3) $\gamma p \to K^0\Sigma^{*+}$

(4) $\gamma p \to (\pi^0 K^0 \Sigma^+)_{n.r.}$

where the $K^{*0}(892)$ decays into $K^0\pi^0$ and the Σ^{*+} decays into $\Sigma^+\pi^0$. The contribution of a non-resonant (n.r.) $K^0\pi^0$ pair in (4) occurs together with a $\Sigma^+(1189)$.

Recent theoretical studies of Σ^+ photoproduction in the channel $\gamma p \to \pi^0 K^0 \Sigma^+$ [11] have been performed using a chiral unitary approach for meson-baryon scattering in the energy range close to 1700 MeV, below the threshold for K^* production. The theoretical model is based on the assumption that the $\Delta^*(1700)$ is excited and decays into $K\Sigma^*(1385)$ or $\eta\Delta(1232)$. It has been applied to calculate the cross sections of the reactions $\gamma p \to p\pi^0\eta$ and $\gamma p \to \pi^0 K^0 \Sigma^+$ [12]. The main conclusion is that the mechanism of both reactions is similar - going through the production of the $\Delta^*(1700)$, which is dynamically generated with strong couplings to the $\eta\Delta$ and $K\Sigma^*$. The current data will be compared with the predictions of this model for the reaction $\gamma p \to \pi^0 K^0 \Sigma^+$.

Quark model predictions for K^* photoproduction via nucleon resonance excitations in the channels $\gamma p \to K^{*0}\Sigma^+$ and $\gamma p \to K^{*+}\Sigma^0$ were presented in Ref. [13]. In the model, resonances are treated as genuine quark states. There are only two free parameters corresponding to the vector and tensor couplings which depend on the quark mass. Using this approach the cross sections for K^* production have been predicted based on SU(3) symmetry and quark coupling parameters extracted from non-strange production like ω meson production. The assumption of t-channel K exchange in this model leads to strong forward peaking of K^{*0} at higher energies (> 2 GeV).

Another theoretical prediction for a t-channel exchange dominated reaction mechanism in K^* photoproduction involves the assumption that the scalar $\kappa(800)$ meson may play an important role [14]. It was demonstrated that K exchange could describe the reaction mechanism in $K^*\Lambda$ production, but for the $K^*\Sigma$ production the contribution from the $\kappa(800)$ meson could be substantial. The results of the CLAS collaboration have also been compared to this theoretical prediction and are in good agreement. Nevertheless, the open question here is the controversial structure of the $\kappa(800)$ meson. We will compare our data to this model too.

Experimentally, $K^{*+}(892)$ photoproduction has been studied with the SAPHIR detector, in the reaction $\gamma p \to K^{*+}\Lambda$ [15]. The K^{*+} was reconstructed from $K^0\pi^+$ where the measured charged particles are $\pi^\pm$ and proton. The differential cross sections show a forward peaking of the K^{*+} meson. The measured total cross section is 0.35 μb at 2.2 GeV incident photon energy.

In recent studies of K^{*0} photoproduction by the CLAS collaboration in the reaction $\gamma p \to K^{*0}\Sigma^+$ [16], the K^{*0} was reconstructed from the detected particles K^+ and π^-; the Σ^+ was treated as missing particle. The angular distributions are forward peaked; good agreement with the quark model of [13] was achieved after a slight adjustment of the vector and tensor K^* couplings to the nucleon. The small enhancement of the cross section at backward angles has been interpreted as effect of s- and u-channel resonances that couple to $K^{*0}\Sigma^+$. The production of higher hyperon resonances Y^*, decaying into $\Lambda\pi$ or $\Sigma\pi$, has overlapping kinematics with K^* production leading to a background for the channel $\gamma p \to K^{*0}\Sigma^+$.

Our data presented here will be compared with predictions of the available theoretical models and with the published experimental results. The reactions (1)-(4) have been identified via the neutral decay channels, which exclude the contamination from hyperon resonances subsequently decaying via Λ production. The contribution from higher Σ^* hyperon resonances, decaying into $\Sigma\pi$, provide an important background to the reaction (2). We will show evidence for identified higher hyperon states. For photon energies above 1850 MeV, Σ production is dominated by reaction (2). Thus it is important to identify the Σ^* contribution against the leading K^* contribution, since they are both leading to the same final state.

This paper is organized as follows: In Section 2 we describe the experiment. Section 3 provides the analysis method and event reconstruction. Section 4 shows how to reconstruct and remove the $p\pi^0\eta$ events which have the same final state and represent a considerable background to the reactions of interest. In Section 5 we discuss the reconstruction of K^0, K^{*0} and Σ^+. The differential and total cross sections are given and discussed in Section 6. The paper is summarised in Section 7.

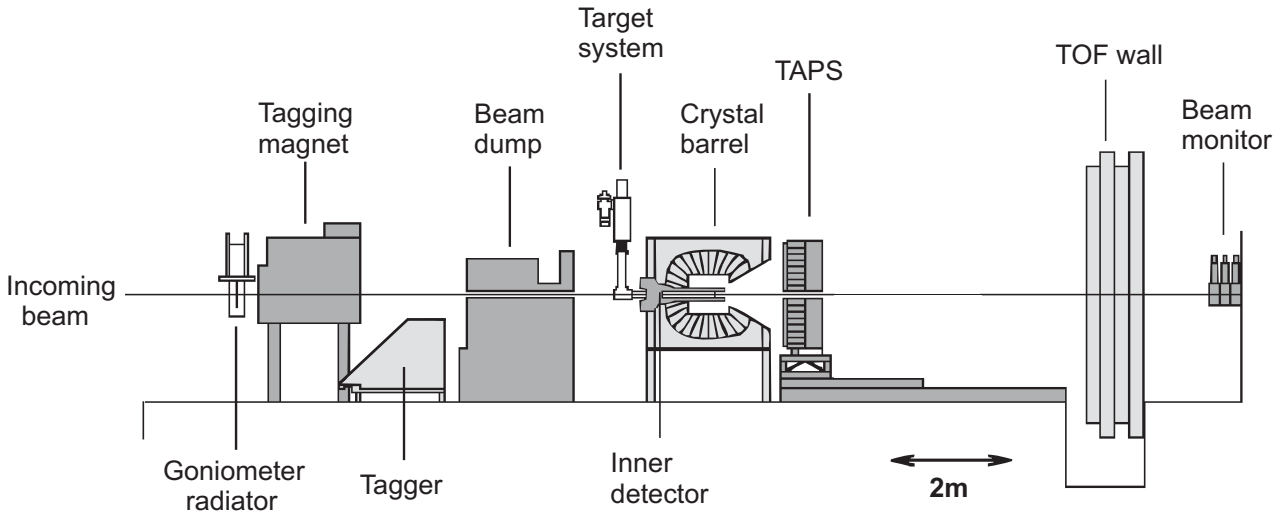

Fig. 1. Sketch of the experimental setup CBELSA/TAPS. The electron beam enters from the left side, hits the radiator and produces bremsstrahlung. The photons are energy tagged and hit the LH_2 target, which is in the center of the Crystal Barrel detector. The TAPS detector is placed just after the CB and serves as a forward wall of the CB. Charged particles leaving the target are identified in the inner scintillating-fibre detector and in the plastic scintillators in front of each BaF_2 crystal in TAPS. A photon counter for the flux determination (γ intensity monitor) is placed further downstream.

2 The experiment

Data have been taken with the detector systems Crystal Barrel (CB) [17] and TAPS [18,19] at the 3.5 GeV electron stretcher facility ELSA [20,21]. The detector setup is shown schematically in figure 1. Electrons extracted from ELSA with energy E_0 hit a primary radiation target, a thin copper or diamond crystal, and produce bremsstrahlung [22]. The tagging system consists of 480 scintillating fibers and 14 partly overlapping scintillator bars. It provides the corresponding energy of the photons ($E_\gamma = E_0 - E_e^-$) from the deflection of the scattered electrons in a magnetic field. Photons were tagged in the energy range from 0.5 GeV up to 2.9 GeV for an incoming electron energy of 3.2 GeV. The total tagged photon intensity was about $10^7\ s^{-1}$ in this energy range. The energy resolution varied between 2 MeV for the high photon energies and 25 MeV for the low photon energies at an electron beam energy of 3.2 GeV. The part of the beam that did not produce any bremsstrahlung photons is deflected by the magnet as well. Since the electrons have retained their full energy the curvature of their track is smaller and they pass over the tagger into a beam dump.

At the end of the beam line a Čerenkov detector consisting of 9 lead glass crystals has been installed (fig. 1) which measures those photons that pass through the target without undergoing an interaction. The information provided from this detector has been used for the photon flux determination (see section 6.1).

The Crystal Barrel detector, a photon calorimeter consisting of 1290 CsI(Tl) crystals (≈16 radiation lengths), covered the complete azimuthal angle and the polar angle from 30^o to 168^o. The liquid hydrogen target in the center of the CB (5 cm in length, 3 cm in diameter) has been surrounded by a scintillating fibre-detector to detect charged particles [23]. The CB has been combined with a forward detector - the TAPS calorimeter - consisting of 528 hexagonal BaF_2 crystals (≈12 X_0), covering polar angles between 5^o and 30^o and the complete 2π azimuthal angle. In front of each BaF_2 module a 5 mm thick plastic scintillator has been mounted for the identification of charged particles. The combined CB/TAPS detector covered 99% of the full 4π solid angle. The high granularity of this system makes it very well suited for the detection of multi-photon final states.

The first level trigger was derived from TAPS, requiring either one or two hits above different thresholds. The second level trigger was based on a fast cluster recognition (FACE) logic, providing the number of clusters in the Crystal Barrel. For part of the data the minimal number of hits in FACE was one, otherwise at least two hits were requested, which did not introduce any bias for the channels analyzed here.

3 Event reconstruction and event selection

The events due to the reactions $\gamma p \to K^{*0}\Sigma^+$ and $\gamma p \to K^0\pi^0\Sigma^+$ were reconstructed from the measured eight photons and the proton in the final channel. Only events containig exactly nine clusters - eight neutral and one additional charged hit - were selected. The charged clusters were identified by using the plastic scintillators in front of the TAPS detector and the fibre detector in the CB. In

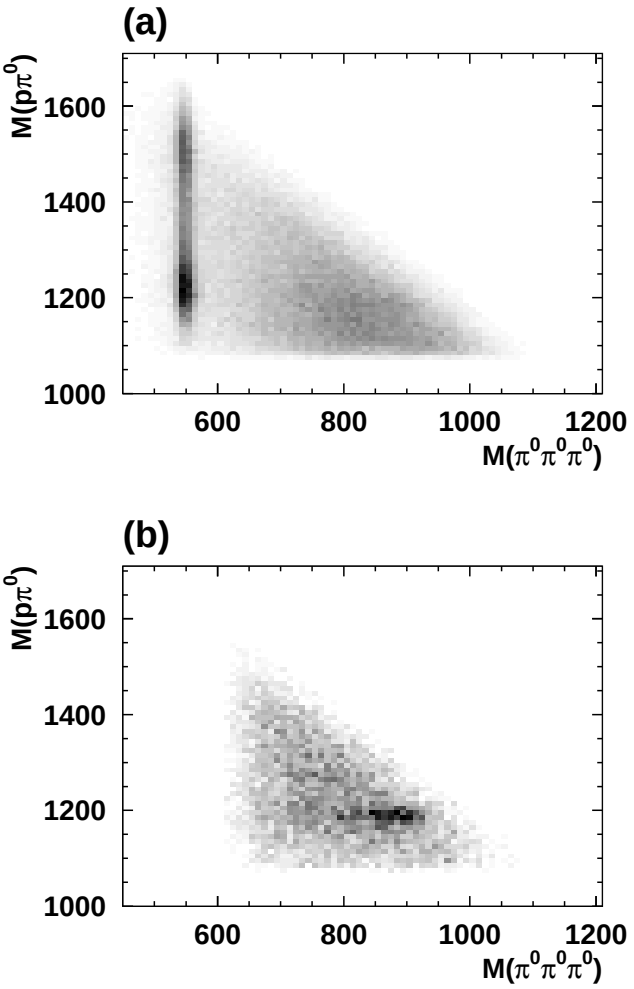

Fig. 2. (a): Invariant mass M(pπ^0) against M($\pi^0\pi^0\pi^0$) in the energy range 2000-2150 MeV, after applying the kinematic fit. The η peak is clearly seen at 547 MeV. The resolution (σ) in M($\pi^0\pi^0\pi^0$) is 9 MeV. (b): After eliminating the events with M($\pi^0\pi^0\pi^0$) $<$ 600 MeV, a peak at M($\pi^0\pi^0\pi^0$) = 896 MeV and M(pπ^0) = 1189 MeV is observed, showing correlated $K^*\Sigma$ production.

order to reduce the background, a cut in a missing mass spectrum derived from the identified eight photons was applied. The cut selected events in the region of the nucleon mass; the width of the missing mass cut varied as a function of the incident photon energy (40 MeV at E_γ = 1 GeV to 120 MeV at E_γ = 2.6 GeV). Events which survived this cut were kinematically fitted to the hypothesis $\gamma p \rightarrow p_{miss}\pi^0\pi^0\pi^0\pi^0$. The procedure is described in detail in [24]. Measurements of the deposited energy and the direction of the photons in the CB and TAPS calorimeters were used in the fit. For the proton, only the two angles of its trajectory were used, its energy was calculated, since the fit is overconstrained. The constraints applied in this analysis are energy and momentum conservation and the invariant masses of the pions.

The confidence level distribution of the fit is shown in

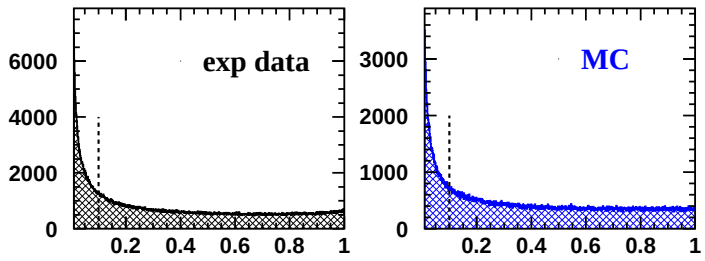

Fig. 3. Confidence level distributions for the kinematic fit to the hypothesis $\gamma p \rightarrow p_{miss}\pi^0\pi^0\pi^0\pi^0$ for experimental data (left) and the corresponding Monte Carlo simulation (right). The dashed verticle line shows the applied cut on the confidence level.

fig. 3. Above 20% the distribution is flat in both data and Monte Carlo events. The combination of γ pairs yielding the highest confidence level was taken as the correct one. Events for which the kinematic fit yielded a confidence level of less than 10% were removed from the data. In order to eliminate time accidental background a prompt coincidence between a photon in TAPS and an electron in the tagger was required. Random time coincidences were subtracted, using events outside the prompt time coincidence window. More details of this procedure can be found in [25].

4 The reaction $\gamma p \rightarrow p\pi^0\eta$

An important competing channel, leading to the same final state is $\gamma p \rightarrow p\pi^0\eta \rightarrow p4\pi^0$. Calculations [12] predicted 30 times larger cross section in comparison to the reactions with Σ^+ production. Experimentally, the cross section for $\gamma p \rightarrow p\pi^0\eta$ reaction was determined to $\sim$4μb [26]. Events with one π^0 and three π^0's from η-decay were selected. The two-dimensional plot of the $p\pi^0$ invariant mass versus that of the $3\pi^0$ system as a result of the 4 possible combinations is shown in fig. 2a. A vertical band for η around 547 MeV can be seen. The $p\pi^0$ invariant mass distribution within the η band exhibits a strong peak due to the $\eta\Delta(1232)$ intermediate state. The results from the analysis of the $p\pi^0\eta$ channel will be published separately. In the present analysis events due to $p\pi^0\eta$ were removed by a cut M($\pi^0\pi^0\pi^0$) $<$ 600 MeV (fig. 2b). After these cuts, 9500 $p4\pi^0$ events remain for the analysis of strangeness production.

5 The yield of hyperon Σ^+, K^0 and K^{*0} mesons

From the $p4\pi^0$ final state, the Σ^+, K^0, and K^{*0}, are reconstructed. The pπ^0 and $3\pi^0$ combinations are shown

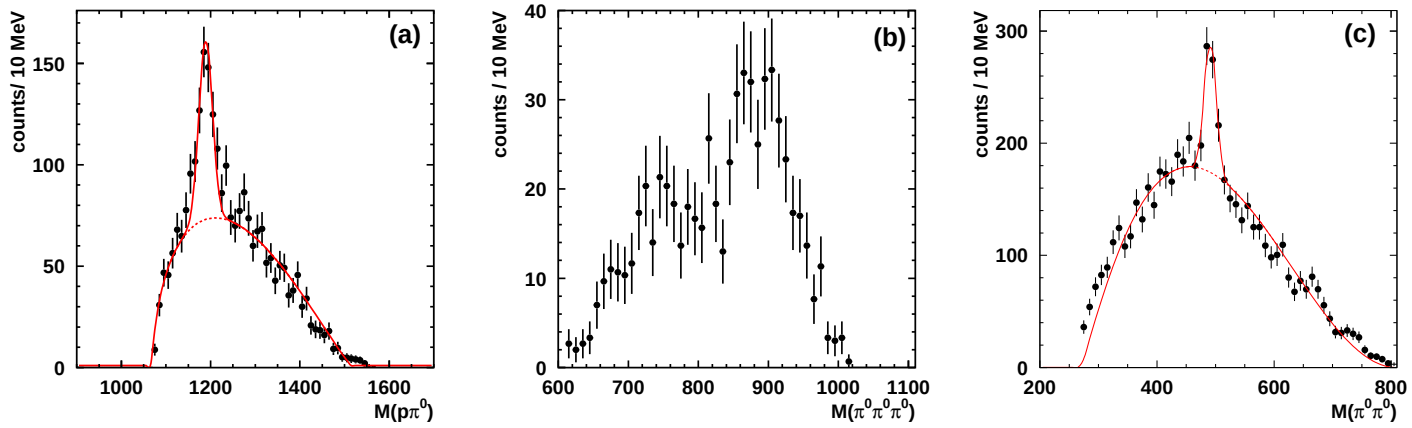

Fig. 4. Projections of fig. 2b on the y-axis (a) and (b) on the x-axis with a cut of 1160-1220 MeV on the $p\pi^0$ invariant mass spectrum (see fig. 2). The incoming photon energies are between 2000 and 2150 MeV. The solid curve shows the fit of the signal and the background. There are 340 events assigned to Σ^+ and 100 events due to K^{*0}. A resolution of 15 MeV (σ) for Σ^+ is given by the fit. The $\pi^0\pi^0$ invariant mass spectrum from all combinations of $4\pi^0$-events, cutting on the $p\pi^0$ invariant mass spectrum from 1160-1220 MeV, is shown in (c). The solid curve shows the fit to the background and the K^0 signal. The fit yields a K^0 mass resolution of 10 MeV (σ). Σ^+ (a) and K^0 (c) yield agree within 10% .

in fig. 2b under the condition that the invariant mass of the $2\pi^0$ from the $3\pi^0$ on the x-axis should be: 470 MeV $< M(\pi^0\pi^0) <$ 520 MeV. This cut has been applied to reconstruct the Σ^+ and K^{*0} which require kaons to be selected (reactions (2), (3) and (4)). A peak at $M(\pi^0\pi^0\pi^0)$ = 896 MeV and $M(p\pi^0)$ = 1189 MeV shows correlated $K^*\Sigma$ production. Figures 4a and 4b present the projections on the $p\pi^0$ and $\pi^0\pi^0\pi^0$ invariant mass axes, respectively. The spectrum in 4a is fitted by a combination of polynomial and Gaussian functions and shows a clear peak at 1189±2.0 MeV, corresponding to Σ^+. The fit yields a resolution σ=15±3.1 MeV. The $\pi^0\pi^0\pi^0$ invariant mass spectrum in 4b, a projection on the x-axis of the two-dimensional plot in fig. 2b with a cut on $M(p\pi^0)$ in 1160-1220 MeV, shows a peak around 896 MeV, corresponding to K^{*0}. Also after applying the cuts a considerable background remains. The background in this spectrum is very complex and is discussed later in this section. The $\pi^0\pi^0$ invariant mass from six different combinations is shown in fig. 4c. All $\pi^0\pi^0$ combinations have been taken into account requiring that one of the other two π^0's and a proton have an invariant mass between 1160 and 1220 MeV, because the kaons are always produced with the Σ^+. The peak at 496 MeV corresponds to K^0 mesons from one of the reactions (2), (3) or (4). Higher lying hyperon states Σ^* could contribute to K^0 production via: $\gamma p \rightarrow K^0\Sigma^* \rightarrow K^0\pi^0\Sigma^+ \rightarrow (\pi^0\pi^0)(\pi^0 p\pi^0)$, where Σ^* could be $\Sigma^*(1385)$ or higher lying Σ^* states decaying into $\pi^0\Sigma^+(1189)$. The threshold for the excitation of $\Sigma^*(1385)$ is E_γ=1400 MeV. The reactions on the proton with neutral mesons only, such as $\gamma p \rightarrow K^0\pi^0\Sigma^+$, excludes Λ's as intermediate states. Requiring the invariant mass $M(p\pi^0)$ to be close to the $\Sigma^+(1189)$ mass, namely between 1160-1220 MeV, figure 5(top) shows a plot of $M(p\pi^0\pi^0)$ versus $M(\pi^0\pi^0)$ for incident photon energies of 2000-2300 MeV. The Σ^+ cut for this plot is important to reconstruct the reaction (3), where Σ^{*+} decays in $\pi^0\Sigma^+$. The vertical band around 500 MeV on the x-axis is from the K^0 events (cf. figure 4c). The projection onto the y-axis, with a cut on $M(\pi^0\pi^0)$ between 470 and 520 MeV is plotted in fig. 5(bottom), which corresponds to a $\pm 2.5\sigma$ cut on the K^0 invariant mass. This cut is shown with solid vertical lines. The non Σ^* background (shaded area in fig. 5) can be determined from side band cuts - shown with the dashed vertical lines on figure 5(top). Left and right from the kaon peak, in the invariant mass range 445-470 MeV and 520-545 MeV, the y-projection of the two-dimensional plot(fig. 5) shows no Σ^* peak (shaded area on fig. 5(bottom). The full spectrum is fitted with a polynomial background and six Breit-Wigner resonance shapes representing the $\Sigma^*(1385)$, $\Sigma^*(1460)$, $\Sigma^*(1560)$, $\Sigma^*(1620)$, $\Sigma^*(1660)$, $\Sigma^*(1670)$ with parameters given by [28]. The position and width of the resonances are taken from [28] and the strengths of the corresponding Breit Wigner are taken as free parameters. As it can be seen the polynomial background (dashed line on fig. 5(bottom)) is in good agreement with the background which we got from the sidebands (shaded area). Apart from the $\Sigma^*(1385)$ no detailed information on the other Σ^* resonances can be extracted due to overlap. The estimated production cross section of the $\Sigma^*(1385)$ resonance is around 0.7±0.3 μb at 1.85 GeV, which is of the same order as observed for the $K\Sigma^*$ channel in [15,27].

Monte Carlo studies have been performed to understand the K^{*0} background [29]. We assumed that the main contribution to the background in K^{*0} spectra is mainly caused by $4\pi^0$ sequential resonance decays and other channels leading to the same final state. The production of higher lying hyperon resonances is hereby of particular importance. Since the final particles produced by $K^0\Sigma^*$ and $K^{*0}\Sigma$ are the same, higher lying hyperon states contribute to the $M(\pi^0\pi^0\pi^0)$ spectra as well. To investigate

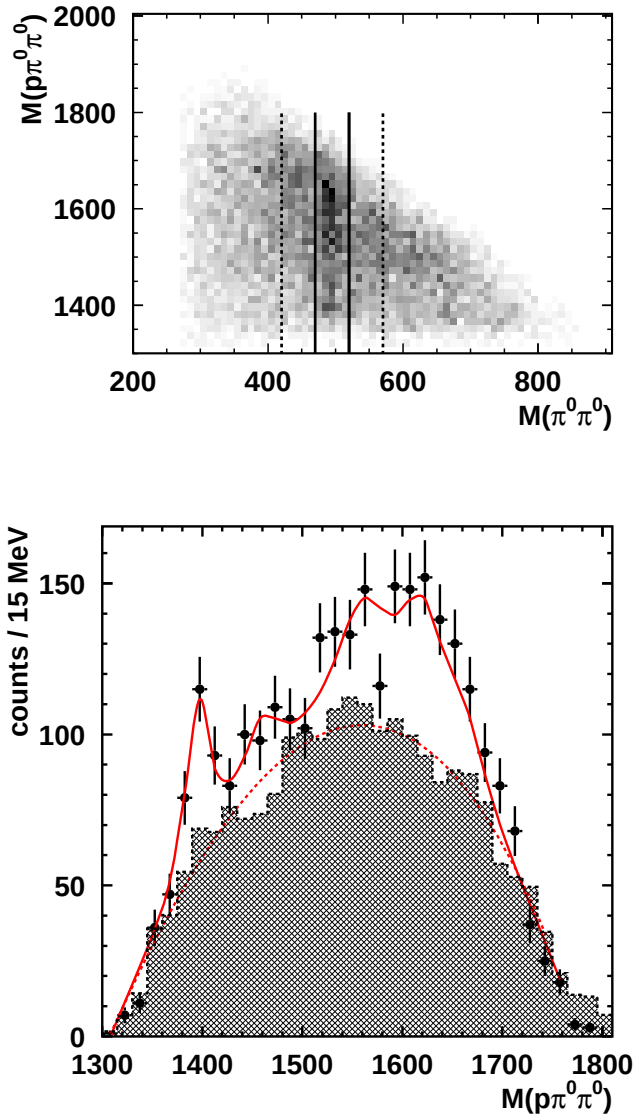

Fig. 5. (top) The invariant mass $M(p\pi^0\pi^0)$ versus the invariant mass $M(\pi^0\pi^0)$, requiring $M(p\pi^0)$ to be between 1160-1220 MeV. The incident photon energy is 2000-2300 MeV. The lines show the cut on $(\pi^0\pi^0)$ invariant mass for the y-projection. (bottom) The projection onto $M(p\pi^0\pi^0)$ axis. The fit function is composed of a polynomial background and Breit-Wigner resonance shapes including $\Sigma^*(1385)$, $\Sigma^*(1460)$, $\Sigma^*(1560)$, $\Sigma^*(1620)$, $\Sigma^*(1660)$ and $\Sigma^*(1670)$ resonances with parameters given by [28]. The shaded area represents the background in the sideband region of K^0, as marked by the dashed lines on the 2-dimensional plot above.

this contribution we have simulated the reaction $\gamma p \rightarrow K^0\Sigma^{*+}(1385)$ and the population of higher Σ^{*+} resonances which decay into $\pi^0\Sigma^+(1189)$. The $3\pi^0$ invariant mass calculated from the K^0 decay pions and the additional pion from the Σ^* decay contributes to the background in the K^{*0} spectra as shown in figure 6. The contribution of $\Sigma^*(1385)$ and higher Σ^* resonances to the background has been normalized to the experimentally observed Σ^* yields. The background below the K^{*0} signal is composed of the Σ^* decay contributions and a 3 body phase space part. The full fit of the experimental $M(\pi^0\pi^0\pi^0)$ spectrum, shown in figure 6, has been done using the K^{*0} signal including the simulated combinatorial background, the background from Σ^*, the 3-body phase space and adjusting their relative magnitudes.

The numbers of the identified Σ^+, K^0, K^{*0} and Σ^{+*} are listed in Table 1 for different photon energy bins. The statistical error of the cross section data has been estimated by $\Delta S = \sqrt{S + 2B}$, where S are the counts in the signal and B are the counts in the background underneath the signal.

Table 1. Σ^+, K^0, K^{*0} and Σ^{+*} counts in different incident photon energy bins (determined by integration of the respective angular distributions)

E_γ (MeV)	$\Sigma^+(1189)$	K^0(without K^*)	K^{*0}	$\Sigma^{*+}(1385)$
1400-1500	16±4	18±5	-	-
1500-1700	77±11	70±13	-	-
1700-1850	92±16	95±19	-	-
1850-2000	244±34	152±39	92±20	30±10
2000-2150	340±35	240±40	100±20	111±25
2150-2300	240±34	146±37	94±15	30±10
2300-2500	290±38	181±40	109±16	16±10
sum	1299±73	902±81	395±36	187±30

6 Results and discussion

6.1 Absolute reaction cross sections

This section describes how the absolute reaction cross sections are determined. The essential ingredients are the reaction yields, the detection efficiency of the individual final states and the photon flux. Due to the almost 4π coverage, the detection efficiency for the hyperon final states is practically independent of the production angle. This is illustrated for both reactions $\gamma p \rightarrow (K^0\pi^0\Sigma^+)_{n.r.}$ and $\gamma p \rightarrow K^{*0}\Sigma^+$ in fig. 7, where the total efficiency is shown, including geometrical acceptance and the detector efficiency. The total efficiency was determined with a GEANT-based Monte Carlo simulation. The simulated events were evenly distributed over the available phase space and analyzed using the same event selection criteria, kinematic fit, applied cuts, thresholds and trigger conditions as for the experimental data. The resulting efficiency varies slightly between 7-10% with the incoming photon energy; its angular dependence is very small.

Uncertainties in the reconstruction of hyperons and vector mesons have been studied. By varying the fit conditions in order to achieve a consistent description of the background in different kinematical regions, an error of 3%

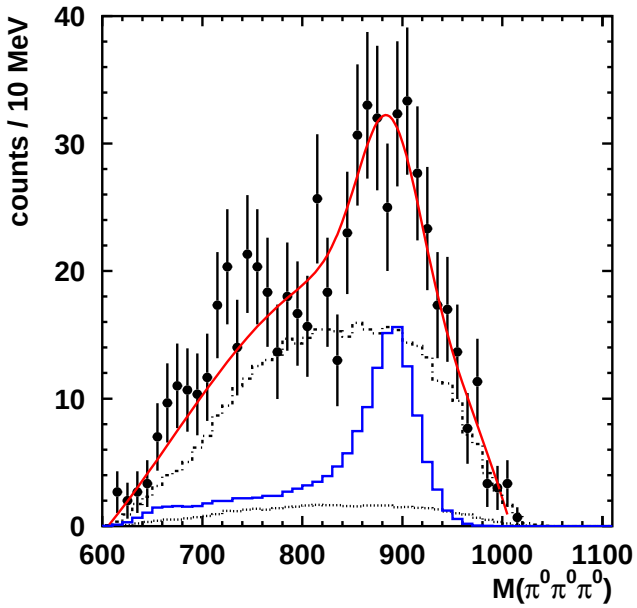

Fig. 6. (Color online) The experimental invariant mass (full black points) $M(\pi^0\pi^0\pi^0)$ for the incident photon energy 2000-2150 MeV. The full fit is shown (red solid curve). The background is described by the contributions from higher Σ^* states (dashed-dotted curve, and the 3-body phase space (dotted curve). The signal shape, including the combinatorial background, is given by the simulation (histogram).

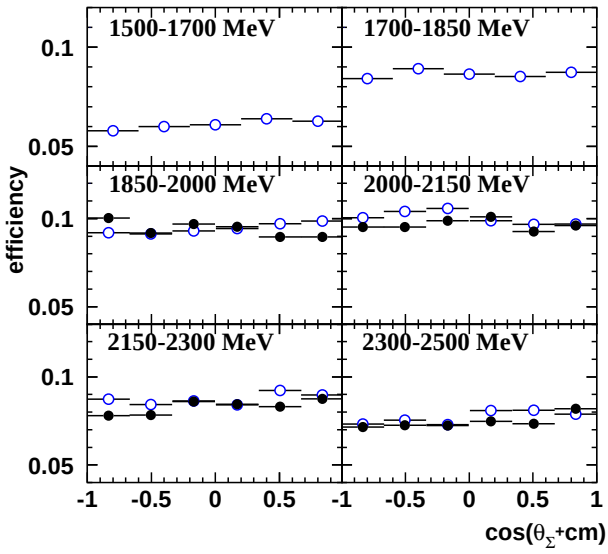

Fig. 7. Total detection efficiency for the reactions $\gamma p \to K^0\pi^0\Sigma^+$ (open circles) and $\gamma p \to K^{*0}\Sigma^+$ (full circles) as a function of the center-of-mass angle of the Σ^+ for different incident photon energy bins.

-15% is deduced.

The photon flux through the target is determined by counting the photons reaching the γ intensity detector in coincidence with electrons registered in the tagger system. This provided an absolute normalization for all measurements. The main point is the accurate determination of the efficiency of the tagging system, as defined by the probability to identify the corresponding photon in the photon beam for each detected electron in the tagger. The γ detector has almost 100% photon detection efficiency. By comparing the number of electrons in the tagging system in coincidence with the number of counts in the γ detector, the tagging efficiency has been determined to vary between 64 to 74 % for different beamtimes. The systematic uncertainty in the cross sections, caused by the photon flux determination has been checked by measurements of known reactions, such as $\gamma p \to p\eta$, and is estimated to be 5%-15% depending on the photon energy.

6.2 Differential cross section

The differential cross sections are calculated from the number of events identified in the respective channel using:

$$\frac{d\sigma}{dcos(\theta^{cm})} = \frac{N_{\Sigma^+}}{A_{\Sigma^+\to p\pi^0}} \frac{1}{N_\gamma \rho_t} \frac{1}{\Delta cos(\theta)} \frac{\Gamma_{total}}{\Gamma_{\Sigma^+\to p\pi^0}} \qquad (1)$$

N_{Σ^+} (N_{K^*}) are the counts of Σ^+ (K^*) determined in different angle and energy bins as described in Sect. 5.

$A_{\Sigma^+\to p\pi^0}$ ($A_{K^*\to K^0\pi^0}$) is the efficiency determined as described in Sect. 6.1;

N_γ is the number of primary photons in the respective energy bin determined as described in Sect. 6.1;

ρ_t is the target area density for the LH_2 target used in this experiment;

$\Delta cos(\theta^{cm})$ is the angle bin width of the angular distributions.

$\frac{\Gamma_{\Sigma^+\to p\pi^0}}{\Gamma_{total}}$ ($\frac{\Gamma_{K^*\to K^0\pi^0}}{\Gamma_{total}}$) is the branching ratio of the reaction $\gamma p \to K^0\pi^0\Sigma^+$ ($\gamma p \to K^{*0}\Sigma^+$) respectively; π^0's were identified via their decay into 2γ which has a relative branching ratio of 98.798%.

The angular distributions for the reactions $\gamma p \to K^0\pi^0\Sigma^+$ and $\gamma p \to K^{*0}\Sigma^+$ are shown in figures 8 and 9, respectively. The results are plotted as a function of $cos(\theta^{cm}_{\Sigma^+})$ and as a function of $cos(\theta^{cm}_{K^*})$ respectively. For incident photon energies higher than 1850 MeV, above the threshold for the K^{*0} production, the cross section for the $\gamma p \to K^0\pi^0\Sigma^+$ has been extracted from the difference between Σ^+ and K^{*0} yields, i.e. $\sigma_{\Sigma K\pi} = \sigma_\Sigma - \sigma_{\Sigma K^*}$.

In the energy range 1500-1850 MeV, below the K^* production threshold, the differential cross section is almost flat. These measurements are in good agreement with the theoretical prediction of [30], based on the model of [12], as shown in the first picture in figure 8. The flat angular distribution indicates dominant s-channel production which is a genuine prediction of a chiral dynamical calculation based on the dominance of the $\Delta(1700)$ in the entrance channel, plus the coupling of this resonance to $K\Sigma^*(1385)$. For the energy region 1500-1850 MeV, where

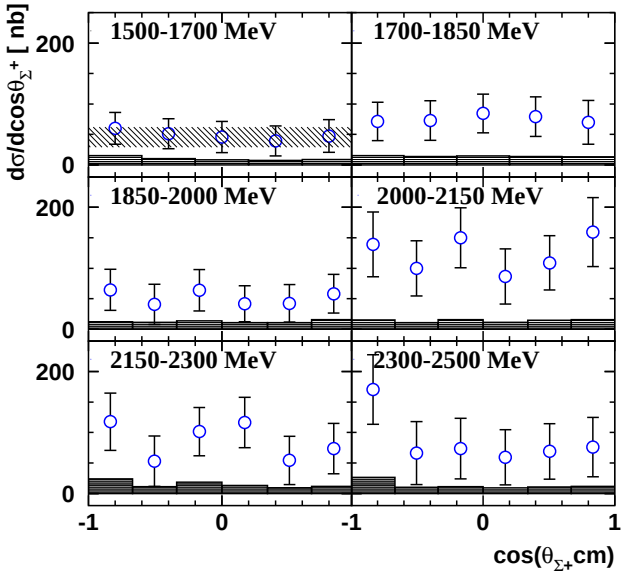

Fig. 8. Differential cross section $d\sigma/\mathrm{d}cos(\theta^{cm}_{\Sigma^+})$ for $\gamma p \rightarrow K^0\pi^0\Sigma^+$. Hereby, the contribution from $K^{*0}\Sigma$ final state has been removed. In the range of energies below the threshold of K^{*0} production the theoretical band for the angular distribution of $\gamma p \rightarrow K^0\pi^0\Sigma^+$ [30] is the shaded area on the first picture. The systematic errors are shown in the boxes on the bottom of each picture.

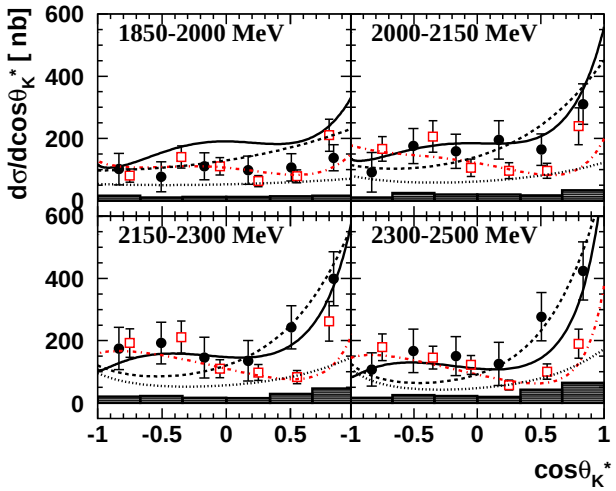

Fig. 9. (Color online) Differential cross section $\gamma p \rightarrow K^{*0}\Sigma^+$ (full circles). The empty squares are the CLAS experimental data [16]. The solid curve represents the theoretical calculations for the $\gamma p \rightarrow K^{*0}\Sigma^+$ reaction in [13,31] with parameters $a = 2,7$ and $b = -1,7$. The dashed and dotted curves denote the calculations in [14] for model II and I respectively. The dashed-dotted curve represents calculations in [31] with free parameters $a = -2,2$ and $b = 0,8$. The grey band on the botom represents the systematic uncertainty.

the K^* production is energetically not possible, the reconstructed $\Sigma^+\pi^0K^0$ events could come from a Δ^* resonance which decays subsequently in $\Sigma^*(1385)K$ and $\Sigma^+\pi^0K^0$. For energies higher than 1850 MeV, an additional contribution from the reaction $\gamma p \rightarrow K^{*0}\Sigma^+$ is possible. These two contributions can be separated experimentally through the $K^0\pi^0$ mass spectrum which exhibits a sharp peak at the position of the K^{*0} meson (fig. 6). The observed counts in the peak at different bins of $cos(\theta^{cm}_{K*})$ are used for the differential cross section determination (fig. 9 full circles).

The differential cross section $\mathrm{d}\sigma/\mathrm{d}cos(\theta^{cm}_{K*})$ for the reaction $\gamma \rightarrow K^{*0}\Sigma^+$ shows a rise in the forward direction when plotted vs the K^{*0} production angle (fig. 9). Production of the K^{*0} meson via t-channel exchange seems to play an important role in the reaction dynamics. These results are compared with the updated calculations from the model in [31], using the free parameters $a = 2.7$ and $b = -1.7$, which describe the universal couplings for the vector and tensor part in the quark vector-meson interaction. These parameters are different from those given in [13], which were derived from ω meson photoproduction based on SU(3) symmetry. Our data are compared to the experimental data from the CLAS collaboration [16] which also show an enhancement in the forward direction. At backward angles we do not observe any rise in the cross section. There is a discrepancy to the CLAS data for the forward angle bins and at incident photon energies higher than 2150 MeV. Our experimental data are consistently higher at angles with $cos(\theta^{cm}_{K*}) > 0.5$ in the lower two pictures in fig. 9.

A comparison to another theoretical model assuming $\kappa(800)$ meson exchange [14] is also shown. The theoretical curves of the so-called model II provide a reasonable agreement with the experimental data which is not the case for model I. The main difference between models I and II of ref. [14] is in the form and the strength of the form factor of the $\kappa(800)$ meson.

The energy dependence of the differential cross sections for the reaction $\gamma \rightarrow K^{*0}\Sigma^+$ is presented in fig. 10 for six angular bins and compared with the experimental data from CLAS. The peaking in the forward direction is more pronounced than in the CLAS data as it can be seen in the lowest two pictures in figure 10.

6.3 t-Scaling

The forward peaking of the $K^{*0}\Sigma^+$ cross section suggests that there is a contribution to the reaction mechanism from t-channel exchange. To test this idea the differential cross section $\mathrm{d}\sigma/\mathrm{d}cos(\theta^{cm}_{K*})$ as function of $cos(\theta^{cm}_{K*})$ was converted to $\mathrm{d}\sigma/dt$ as a function of $t - t_{min}$. The variable t is the Mandelstam invariant that gives the 4-momentum squared of the exchange particles. Since the momentum transfer is limited by kinematics, t lies between t_{min} and t_{max}, given by:

$$t_{min,max} = \left[\frac{m^2_{K*}}{2\sqrt{s}}\right]^2 - \left[\frac{s - m^2_p}{2\sqrt{s}} \mp \sqrt{\frac{(s + m^2_{K*} - m^2_p)^2}{4s} - m^2_{K*}}\right]^2 \quad (2)$$

The cross section $\mathrm{d}\sigma/dt$ is shown in fig. 11. The straight lines represent fits of $e^{a+b|t-t_{min}|}$ in the region below 1.0

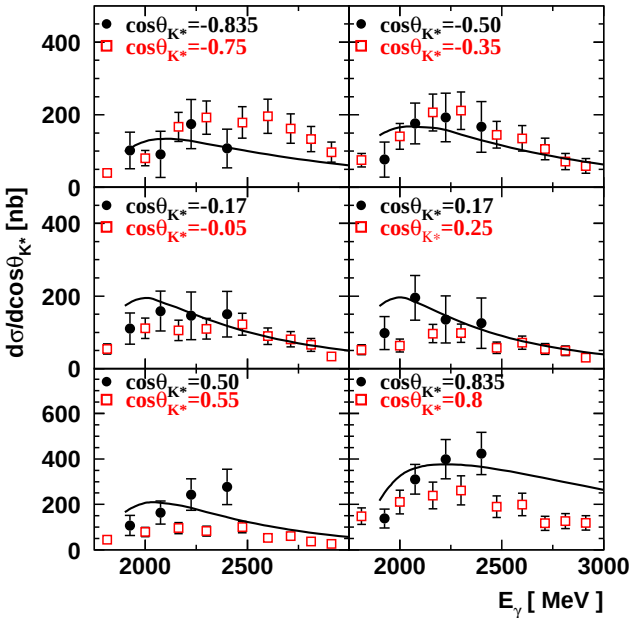

Fig. 10. Differential cross sections for the reaction $\gamma p \rightarrow K^{*0}\Sigma^+$ as a function of the incident photon energy for the angular bins shown in fig. 9. Our experimental data (full circles) are compared to the CLAS data (empty squares) [16]. The solid curve refers to theoretical prediction for the $\gamma p \rightarrow K^{*0}\Sigma^+$ reaction in [31].

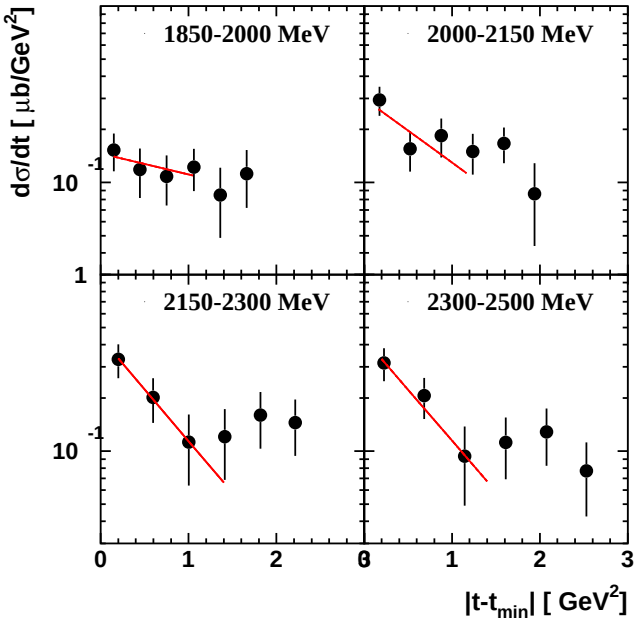

Fig. 11. Differential cross section $d\sigma/\mathrm{dt}$ for $\gamma p \rightarrow K^{*0}\Sigma^+$. For small values of momentum transfer the data are fitted by an exponential function $e^{a+b|t-t_{min}|}$.

GeV^2 of $|t - t_{min}|$. The slope parameter b has a negative value. We plot the slope parameter $-b$ as a function of the incident photon energy E_γ in fig. 12. It can be seen that the slope parameter rises with the photon energy. This is an indication for an increasing contribution to K^{*0} production via t-channel exchange as predicted in [13].

6.4 Total cross section

The total cross sections for the $\gamma p \rightarrow K^0\pi^0\Sigma^+$ and $\gamma p \rightarrow K^{*0}\Sigma^+$ reactions are shown in fig. 13. The cross sections agree within errors with those determined by integrating over the differential cross sections. The experimental cross section for the $\gamma p \rightarrow K^{*0}\Sigma^+$ channel are in reasonable agreement with theoretical predictions of reference [13] with the assumption of a t-channel K^0 exchange.
The predicted total cross section for $K^0\pi^0\Sigma^+$ in [12] is given by a band (the shaded area in fig. 13). The good agreement between theory and experiment suggests that the dynamics used in the model is reasonable for the corresponding energy region. The cross section for $\gamma p \rightarrow K^0\pi^0\Sigma^+$ rises with increasing photon energy. Above 1850 MeV the dominating channel for Σ^+ production is obviously $\gamma p \rightarrow K^{*0}\Sigma^+$. It is about factor 2 larger than the cross section of the $\gamma p \rightarrow K^0\pi^0\Sigma^+$ reaction which includes excited hyperon decays into the $\Sigma^+(1189)$.

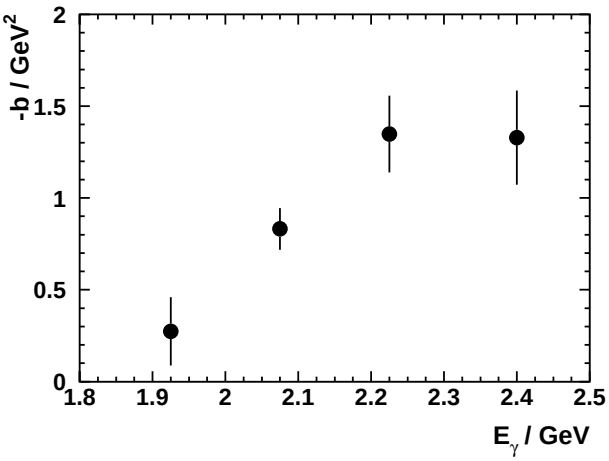

Fig. 12. The slope parameter $-b$ of $e^{a+b|t-t_{min}|}$ as a function of the beam energy E_γ. The error bars include the uncertainties on the slope fits shown in fig. 11.

7 Summary

We have reported measurements of differential and total cross sections for the $\gamma p \rightarrow K^0\pi^0\Sigma^+$ and $\gamma p \rightarrow K^{*0}\Sigma^+$ reactions. The experimental data have been compared with the available theoretical predictions. At low incident photon energies below the K^{*0} production threshold ($E_\gamma <$ 1850 MeV) only the $K^0\pi^0\Sigma^+$ channel is energetically possible, exhibiting a flat angular distribution, dominated by s-channel production which is the prediction based on the dominance of the $\Delta(1700)$, subsequently decaying into $K\Sigma^*(1385)$.

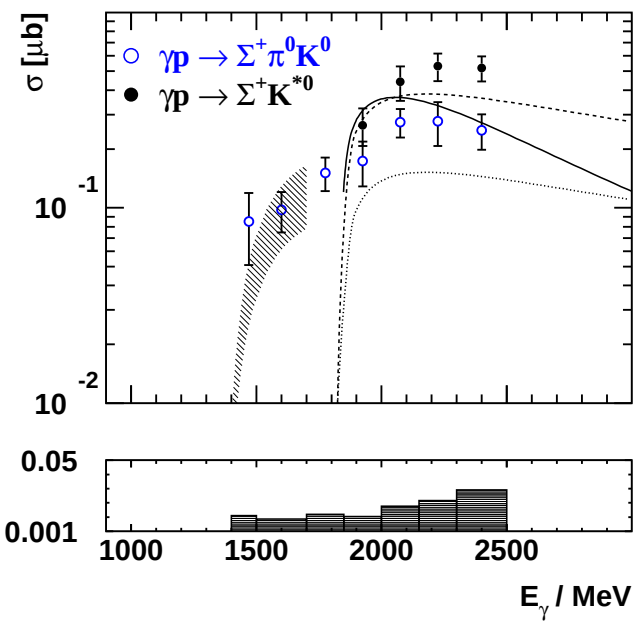

Fig. 13. (Color online) The energy dependence of the total cross sections for $\gamma p \rightarrow K^0\pi^0\Sigma^+$ (empty circles) and $\gamma p \rightarrow K^{*0}\Sigma^+$ (filled circles). The shaded area represents a band for the predicted values from the theoretical calculations of the $\gamma p \rightarrow K^0\pi^0\Sigma^+$ reaction in [12]. The solid curve refers to theoretical prediction for the $\gamma p \rightarrow K^{*0}\Sigma^+$ reaction in [13]. The dashed and dotted curves are the calculations with κ meson exchange [14] in the t-channel, model II and model I, respectively. The systematic errors are shown as an error band on the bottom.

For energies above 1850 MeV the Σ^+ production is mainly associated with K^{*0} production. The angular distributions for the reaction $\gamma p \rightarrow K^{*0}\Sigma^+$ show a rise in the forward direction of the vector meson which indicates a t-channel exchange contribution to the reaction mechanism. It is, however, not yet possible to make an explicit conclusion about the exchanged particle, due to the significant contribution to the $K^0\pi^0\Sigma^+$ channel from the Σ^{*+} production.

The presented data provide valuable confirmation of the theoretical predictions concerning the reaction mechanism of the $\gamma p \rightarrow \pi^0 K^0\Sigma^+$ and $\gamma p \rightarrow K^{*0}\Sigma^+$ reactions. $\Sigma^*(1385)$ and higher Σ^* resonances have been observed in the $\Sigma^+\pi^0$ decay channel. On the basis of existing data we have estimated the production cross section of the $\Sigma^*(1385)$ resonance. A corresponding value for the cross section of the higher Σ^* states photoproduction can not be given because of the overlap of these resonances. Further experiments are required to study the higher Σ^* resonances. Polarisation experiments will be needed to clarify details of the strangeness production process.

8 Acknowledgements

We thank the accelerator group of ELSA as well as the technicians of the participating institutions for their outstanding support. We acknowledge illuminating discussion with Kenneth Hicks on details of the data analysis. Useful discussions with E. Oset and M. Döring and also Q. Zhao on the theoretical interpretation of the data are also highly acknowledged. This work was supported by Deutsche Forschungsgemeinschaft SFB/TR16 and Schweizerischer Nationalfond.

References

1. S. Capstick and W. Roberts, Prog. Part. Nucl. Phys. **45**, 241 (2000).
2. S. Capstick and W. Roberts, Phys. Rev. D **57**, 4301 (1998).
3. R. Lawall *et al.*, Eur. Phys. J. A **24**, 275 (2005).
4. M. Sumihama *et al.*, LEPS Collaboration, Phys. Rev. C **73**, 035214 (2006).
5. R. Castelijns *et al.*, CBELSA/TAPS Collaboration, Eur. Phys. J. A **35**, 39 (2008).
6. R. Bradford *et al.*, CLAS Collaboration, Phys. Rev. C **73**, 035202 (2007).
7. R. Bradford *et al.*, CLAS Collaboration, Phys. Rev. C **75**, 035205 (2007).
8. A. V. Sarantsev *et al.*, Eur. Phys. J. A **25**, 441 (2005).
9. A. V. Anisovich *et al.*, arXiv: hep-ph/07073596
10. S. Capstick and W. Roberts, Phys. Rev. D **58**, 074011 (1998).
11. M. Döring, E. Oset, D. Strottman, Phys. Rev. C **73**, 045209 (2006).
12. M. Döring, E. Oset, D. Strottman, Phys. Lett. B **639**, 59-67 (2006).
13. Q. Zhao, J. S. Al-Khalili, C. Bennhold, Phys. Rev. C **64**, 052201 (2001).
14. Y. Oh and H. Kim, Phys. Rev. C. **74**, 015208 (2006).
15. F. Wieland, Ph.D. thesis University of Bonn, Bonn, Germany (2005).
16. I. Hleiqawi *et al.*, CLAS Collaboration, Phys. Rev. C **75**, 042201 (2007), Erratum-ibid.C76:039905, 2007. /corrected values, see: arXiv: nucl-ex/0701036v3.
17. E. Aker *et al.*, Nucl. Instr. and Methods A **321**, 69 (1992).
18. R. Novotny *et al.*, IEEE Trans. Nucl. Sci.**38**, 392 (1991).
19. A.R. Gabler *et al.*, Nucl. Instr. and Meth. A **346**, 168 (1994).
20. D. Husmann, W. J. Schwille, Phys. Bl. **44**, 40 (1988).
21. W. Hillert, Eur. Phys. J. A **28**, s01, 139 (2006).
22. D. Elsner *et al.*, CBELSA/TAPS Collaboration , Eur. Phys. J. A **33**, 147 (2007).
23. G. Suft *et al.*, Nucl. Instr. Meth., A **538**, 416 (2005).
24. H. van Pee *et al.*, Eur. Phys. J. A **31**, 61 (2007).
25. D. Trnka, Ph.D Thesis University of Giessen, Giessen, Germany (2006).
26. I. Horn *et al.*, CBELSA Collaboration, arXiv: nucl-ex/07111138.
27. L. Guo and D. P. Weygand, CLAS Collaboration: *Proceedings of the Workshop on the Physics of Excited Nucleons NSTAR 2005, Florida State University, Tallahassee, 12-15 October 2005*, edited by S. Capstick *et al.* (World Scientific, Singapore, 2006) p. 306.
28. W. M. Jao *et al.*, Particle Data Group, J. of Physics G **33**, 1049 (2006).

29. M. Nanova for CBELSA/TAPS Collaboration: *Proceedings of the Workshop on the Physics of Excited Nucleons NSTAR 2005, Florida State University, Tallahassee, 12-15 October 2005*, edited by S. Capstick *et al.* (World Scientific, Singapore, 2006) p. 359.
30. M. Döring, Ph.D Thesis University of Valencia, Valencia, Spain (2006).
31. Q. Zhao, *Numerical fit by the quark model of Ref. [13] to the CBELSA/TAPS data*, private communication.